CHINESE OPTICS LETTERS

Vol. 21, No. 7 | July 2023

Detecting the vector of nanoscale light field with atomic defect

Qiyu Wang (王启宇)[1,2], Zehao Wang (王泽昊)[1,2], Xiangdong Chen (陈向东)[1,2,3*], and Fangwen Sun (孙方稳)[1,2,3]

[1] CAS Key Laboratory of Quantum Information, University of Science and Technology of China, Hefei 230026, China

[2] CAS Center for Excellence in Quantum Information and Quantum Physics, University of Science and Technology of China, Hefei 230026, China

[3] Hefei National Laboratory, University of Science and Technology of China, Hefei 230088, China

*Corresponding author: xdch@ustc.edu.cn

Received December 20, 2022 | Accepted April 18, 2023 | Posted Online July 11, 2023

Modulation of a vector light field has played an important role in the research of nanophotonics. However, it is still a great challenge to accurately measure the three-dimensional vector distribution at nanoscale. Here, based on the interaction between the light field and atomic-sized nitrogen-vacancy (NV) color center in diamonds, we demonstrate an efficient method for vectorial mapping of the light-field distribution at nanoscale. Single NV centers with different but well-defined symmetry axes are selected and then interact with the same tightly focused light field. The excitation of a single NV center is related to the angle between the NV center axis and the polarization of the light field. Then the fluorescence patterns of different NV centers provide the information on the vectorial light field distribution. Subsequently analyzing the fluorescence patterns with the help of a deep neural network, the intensity and phase of the light-field vectorial components are fully reconstructed with nanometer resolution. The experimental results are in agreement with theoretical calculations. It demonstrates that our method can help to study light–matter interaction at nanoscale and extend the application of vector light fields in research on nanophotonics.

Keywords: light-field measurement; nitrogen-vacancy center; tightly focused light field.
DOI: 10.3788/COL202321.071202

1. Introduction

High-precision vector light-field manipulation has been widely studied in both fundamental physics and applied optics, such as superresolution imaging[1–3], nanoplasmonics[4–6], and topological photonics[7–10]. The exact knowledge of the vectorial light-field distribution at nanoscale is particularly important for characterizing light–matter interaction and optimizing the generation of a complex light field. Several methods have been proposed to detect vectorial light-field distributions with high spatial resolution. For example, the knife-edge technique[11,12] and near-field scanning optical microscope[13–15] use scanning sharp edges or small tips to obtain the vectorial distributions of a light field with subwavelength resolution. However, the measurements strongly depend on the geometry and material of probes[16]. In addition, the movement of an external tip might induce perturbation to the light field. This high requirement on the quality of the probes and the experimental process limits the applications of these methods.

Recently, single-photon emitters, such as single molecules and color centers, have emerged as a platform to study light–matter interaction at nanoscale[17–21]. As one of the most promising candidates, the nitrogen-vacancy (NV) center in a diamond with stable photophysical properties has been applied for high-resolution electromagnetic field sensing and imaging[22–25]. Especially, the detection of magnetic field vectors at nanoscale has been demonstrated with NV centers of different but well-defined symmetry axes[26–29].

In this work, we use single NV centers in a bulk diamond as sensors to detect the vectorial light–field distribution under the tight focus conditions. Single NV centers of different symmetry axes are selected and interact with the same light field. Since the nonresonant excitation of an NV center is related to the angle between the symmetry axis and the light-field vector, different fluorescence patterns that contain the vectorial information on the light field are collected with different NV centers. By analyzing the fluorescence patterns of different types of single NV centers with the help of a deep neural network, the intensity and phase of light-field vector components can be fully reconstructed. The results match the theoretical expectation. It demonstrates that the atomic-sized NV center can be used as a probe to detect the vectorial light field with high spatial resolution and low perturbation. This technique can help to optimize the

generation of a complex light field and study light–matter interaction at nanoscale.

2. Methods and Experimental Results

The principle of our method is shown in Fig. 1(a). The size of an NV center is actually much smaller than the size of a vector light field. In order to express the principle of our method more clearly, the sizes of NV centers are deliberately enlarged in Fig. 1(a). The optical excitation efficiency of a single NV center is related to the angle between the NV center's symmetry axis and the polarization of a light field[30,31]. One example of the polarization-dependent excitation of a single NV center is shown in Fig. 1(b), where a linearly polarized light beam is used to pump the NV center. The corresponding symmetry axis of the single NV center is shown in Fig. 1(c). We can see that the collected fluorescence intensity changes with the polarization of excitation. By selecting NV centers with different axes and scanning the relative positions between NV centers and the light field, a series of fluorescence patterns can be obtained. Each pattern contains part of the vectorial light-field distribution information. Combining the information from the measurement with different NV centers, the vectorial distributions of the light field can be fully reconstructed.

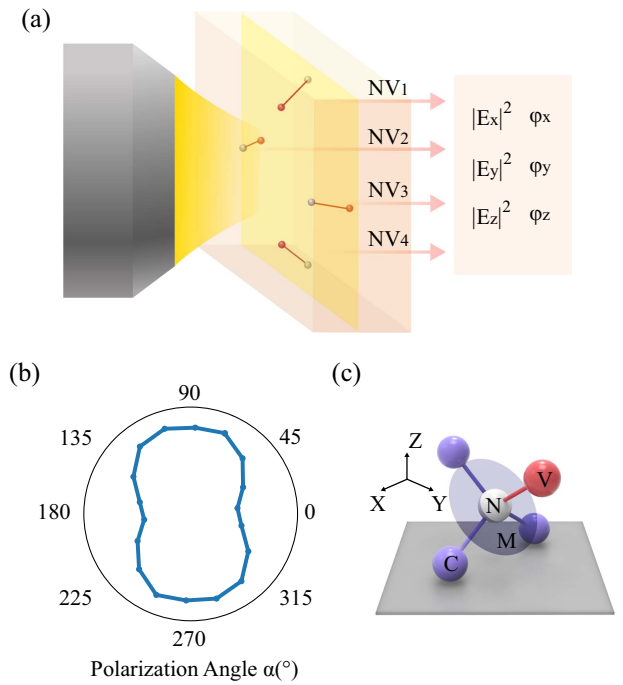

Fig. 1. (a) Principle of using NV centers to detect the vectorial distributions of a light field. The single NV centers with different but well-defined axes interact with the same light field. The corresponding fluorescence emission is then analyzed to obtain the vectorial distributions of the light field. (b) Normalized fluorescence intensity of the single NV center versus the x–y plane laser polarization angle α. $\alpha = 0°$ corresponds to x axis. (c) Diagram of the NV center with symmetry axis of $[0, \frac{\sqrt{6}}{3}, \frac{\sqrt{3}}{3}]$. The white sphere represents the nitrogen atom, the red sphere represents the vacancy, and the blue sphere represents carbon atom. The translucent circle represents the surface perpendicular to the NV center axis and is noted as M.

A [100] surface and ⟨110⟩ edge single-crystal diamond plate that contains four types of NV centers with different axes is applied in this work to detect the vector light field. Single NV centers are produced through low dosage nitrogen ion implanting and subsequent annealing. The depth of NV centers is estimated to be approximate 20 nm. The NV centers with different axes are identified through electron spin resonance spectrum. As an example, one of the four possible NV centers in the diamond plate is shown in Fig. 1(c). The x and y axes are defined according to the edges of the plate. The light field propagates along the direction of the z axis in our experiments. The symmetry axis of the NV center in Fig. 1(c) is $[0, \frac{\sqrt{6}}{3}, \frac{\sqrt{3}}{3}]$. The plane perpendicular to this axis can be written as $\sqrt{2} \cdot y + z = 0$ and is noted as M. According to previous research[31–33], the fluorescence intensity radiated by the NV center is proportional to the projection of the excitation light-field vector in the M-plane. The fluorescence emission of a single NV center under the excitation of a light field $\vec{E}$ can be calculated as[30,34]

$$I_j \propto |(\overrightarrow{\mathrm{NV}_j} \times (\vec{E} \times \overrightarrow{\mathrm{NV}_j}))|^2, \qquad j = 1, 2, 3, 4. \tag{1}$$

$\overrightarrow{\mathrm{NV}_j}$ presents the orientation of the NV center axis. For the diamond used in this work, all the four possible orientations of NV center axes are expressed as follows:

$$\overrightarrow{\mathrm{NV}_1} = \left[0, \frac{\sqrt{6}}{3}, \frac{\sqrt{3}}{3}\right], \tag{2}$$

$$\overrightarrow{\mathrm{NV}_2} = \left[0, -\frac{\sqrt{6}}{3}, \frac{\sqrt{3}}{3}\right], \tag{3}$$

$$\overrightarrow{\mathrm{NV}_3} = \left[\frac{\sqrt{6}}{3}, 0, -\frac{\sqrt{3}}{3}\right], \tag{4}$$

$$\overrightarrow{\mathrm{NV}_4} = \left[-\frac{\sqrt{6}}{3}, 0, -\frac{\sqrt{3}}{3}\right]. \tag{5}$$

Therefore, by recording emission of these four types of NV centers, we can obtain four equations about the light-field vector $\vec{E}$. Mathematically, the light-field vector consists of the squared electric field components $|E_x|^2$, $|E_y|^2$, and $|E_z|^2$ and the phases φ_x, φ_y, and φ_z. It means that four equations are not sufficient to directly solve the light-field vector. Here, we consider that the to-be-detected light field is generated under the tight focus condition. Taking this prior knowledge to deduce the vectorial light-field distribution, the six unknown variables of the vector light field can be solved by the sensing results from the four different NV centers. We combine the prior knowledge and the neural network to reconstruct the vectorial light distribution. This technique is called deep physics prior (DPP). Untrained generative models are a class of machine-learning

methods for image reconstruction, such as deep image prior[35] and deep decoder[36]. These models do not require any training data, and only test samples to learn. For example, deep image prior uses a generative network for image reconstruction, usually a convolutional neural network. The input of the generative network makes a fixed random vector; the error function is defined as the difference between the output of the generative network and the test sample. By training deep image prior, tasks such as image denoising, image restoration, and superresolution imaging can be accomplished with high performance.

We introduce the light-field focusing and NV center sensing into the deep image prior model to construct the DPP architecture. The input to the model is a random vector, and the intensity and phase of free-space light are output through a fully convolutional neural network (FCN). The free-space light goes through a physical process [tightly focused by a high numerical aperture (NA) object], which is an angular spectral integration in mathematics, followed by the output of the vector distributions of the light field under tight focus conditions. DPP directly models the entire physical process of NV centers interacting with the tightly focused light field and is embedded in the deep image prior architecture. The physical process forms a constraint on the solution as prior knowledge, allowing us to solve the vector light-field distribution with an insufficient number of equations. The DPP deep neural network overview is shown in Fig. 2(a).

To verify our method, we use NV centers to detect the tightly focused radially polarized beam, which has been extensively studied in optical storage[37,38], laser machining[39], and optical trapping[40,41]. Based on the theory of focusing of polarized beams, when the radially polarized beam is tightly focused by a high NA objective, the electric field in the focal plane can be written as[42,43]

$$E_r(r,z) = A\int_0^{\alpha} \cos^{1/2}\theta \, \sin(2\theta) l(\theta) J_1(kr\,\sin\theta) e^{ikz\cos\theta} \mathrm{d}\theta, \quad (6)$$

and

$$E_z(r,z) = 2iA\int_0^{\alpha} \cos^{1/2}\theta \sin^2\theta l(\theta) J_0(kr\,\sin\theta) e^{ikz\cos\theta} \mathrm{d}\theta. \quad (7)$$

E_r and E_z represent the radial and longitudinal components of the electric fields, respectively. The upper limit of integral $\alpha = \arcsin(\mathrm{NA}/n)$. J_0 and J_1 are the Bessel function of the first kind. $k = 2\pi/\lambda$ is the wavenumber of the beam in the medium. A is the strength at the pupil aperture. The function $l(\theta)$ describes a Bessel–Gaussian beam, which can be expressed as[42]

$$l(\theta) = \exp\left[-\beta^2\left(\frac{\sin\theta}{\sin\alpha}\right)^2\right] J_1\left(2\beta\frac{\sin\theta}{\sin\alpha}\right), \quad (8)$$

where β is the ratio of the pupil's radius and the beam waist, which we take as unity in our configuration. Considering boundary conditions at the interface, the transverse component of the electric fields has to be continuous across the diamond interface.

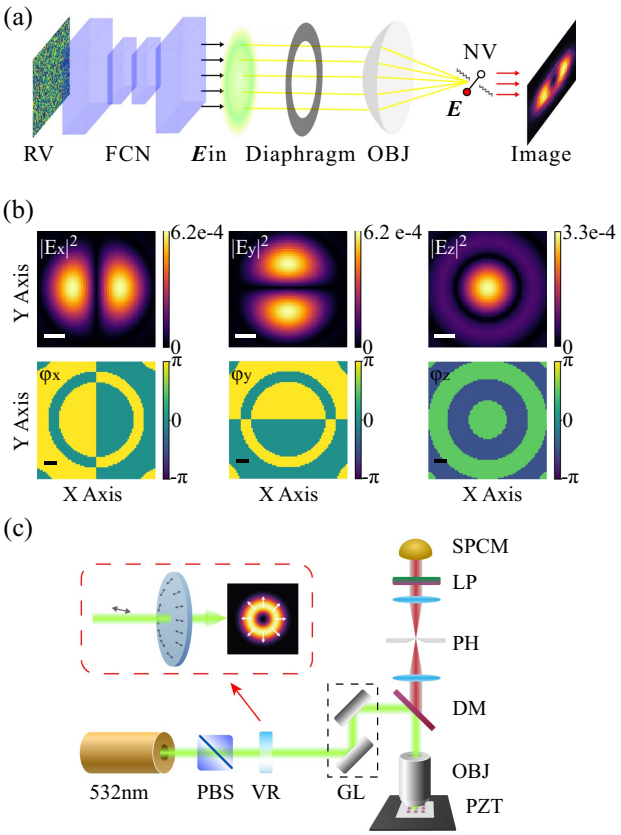

Fig. 2. (a) DPP deep neural network overview. RV, random vector; OBJ, objective. (b) Calculated intensity and phase distributions of the radially polarized beam in the focal plane under the tight focus condition (NA = 0.9). The intensity distribution results are normalized by total intensity. (c) Schematic of the experimental setup with a home-built confocal nanoscopy. PBS, polarization beam splitter; VR, vortex retarder; GL, galvo scanning mirrors; SPCM, single-photon counting module; LP, long-pass filter; DM, dichroic mirror; OBJ, objective; PZT, piezoelectric displacement table. Scale bars in (b) are 200 nm.

However, the longitudinal component of electric fields changes when entering the diamond[44], which can be written as

$$E_{z1}\varepsilon_1 = E_{z2}\varepsilon_2. \quad (9)$$

E_{z1} is the z component of the electric fields near the diamond surface in air, and ε_1 is air relative permittivity. E_{z2} is the z component of electric fields' inner diamond, and ε_2 is the diamond relative permittivity. Therefore, the change in refractive index caused by the diamond will decrease the E_z component. Based on the study of focusing near the planar interface[44], we use the angular spectrum integration method to calculate numerical solutions of the vector light distribution generated by NV centers inside the diamond interacting with a radially polarized beam under tight focus condition. The calculated values are shown in Fig. 2(b).

The experimental detection of the light field is performed with a home-built confocal microscopy system, as shown in Fig. 2(c). A 532 nm laser passes through a polarization beam splitter and transform into a p-polarized beam. The beam is then sent to a vortex retarder (Thorlabs, WPV10L-532). The fast axis of the

vortex retarder is aligned with the direction of the beam polarization. The radially polarized beam is then generated and focused on the NV center by an objective (NA = 0.9). The objective is also used to collect the fluorescence of the NV center. The fluorescence radiated by the NV center is separated by a long-pass dichroic mirror (edge wavelength 555 nm) and then sent to a pinhole. The pinhole can prevent background from the out-of-focus plane. Finally, the fluorescence of the NV center is collected by a single photon-counting module after passing through a long-pass filter (edge wavelength 647 nm). A piezoelectric displacement table is used to place the diamond and to select the NV centers with different axes. In this way, the fluorescence patterns of single NV centers with different axes are obtained. Since the position of the NV center is fixed during scanning, the variation of the collecting point spread function can be ignored. The collected fluorescence intensity would be determined by the interaction between the NV center and the to-be-detected light field.

The fluorescence patterns generated by NV centers with four different axes are shown in Fig. 3. Four different types of NV centers are labeled as NV_1, NV_2, NV_3, and NV_4 in Fig. 3(a). The corresponding fluorescence patterns are shown in Fig. 3(b). The pixel size of the images is approximately 34 nm, which is limited only by the accuracy of the scanning mirror. The results are a match with the numerical simulations of fluorescence emission under the excitation of a tightly focused radially polarized beam [Fig. 3(c)]. The small difference between the experimental measurements and calculation values might be caused by uncontrollable mechanical vibrations during the scanning process, the imperfection of the tightly focused light-field distribution, and the background noise.

With the assistance of the DPP deep neural network, the three-dimensional vector field distribution of the radially polarized beam under the tight focus condition is reconstructed in Fig. 4. The intensities of the x and y components in the focal plane both show two semicircular symmetric distributions. For the intensity distribution of the z component, there is a bright spot in the center, surrounded by a weaker ring. As for phase distributions, there is a significant difference between the left and right sides of the x component and a significant difference between the top and bottom sides of the y component. For the z component, there is a significant difference between the inner and outer circles. Meanwhile, we can clearly observe there exists around 0.49π difference at the center in the φ_z distribution compared to the φ_x and φ_y distribution, where the theoretical value is 0.5π. The phase reconstruction results show a lower signal-to-noise ratio at the edge of the three components. This is because NV fluorescence intensities in these areas are weak. The reconstruction results are in general consistent with the theoretical calculation values in Fig. 2(b), which demonstrate that our method can detect the three-dimensional vector light-field distribution with high spatial resolution. In the future, we will further improve the accuracy of our method by optimizing the experimental system and improving the NV center fluorescence counting.

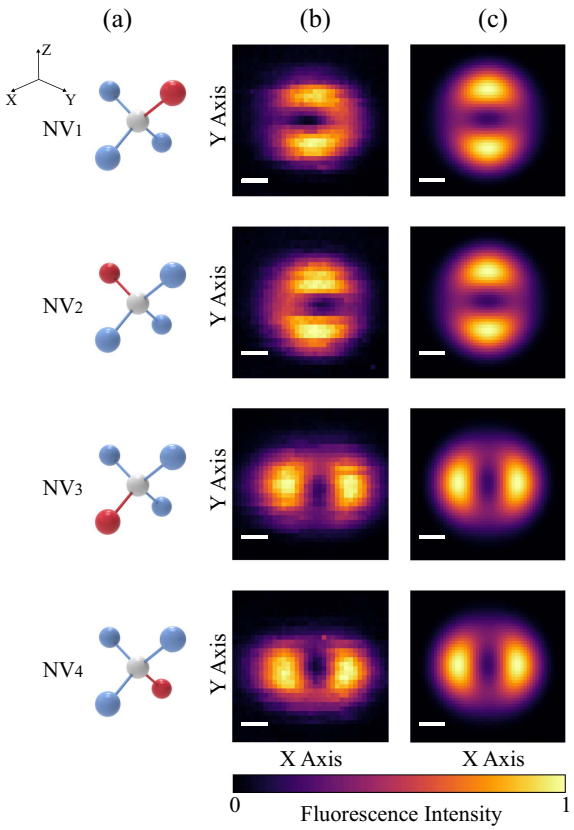

Fig. 3. (a) Four NV centers with different axes in the [100]-oriented diamond are used to detect the light field. The corresponding coordinate system is set near NV_1. (b) Experimentally obtained fluorescence patterns in the focal plane with the excitation of a radially polarized beam; the fluorescence is recorded with the NV centers in (a). (c) Theoretical estimated fluorescence patterns of NV centers in the focal plane; the fluorescence intensities are normalized by the maximum value in each image. Scale bars in (b) and (c) are 200 nm.

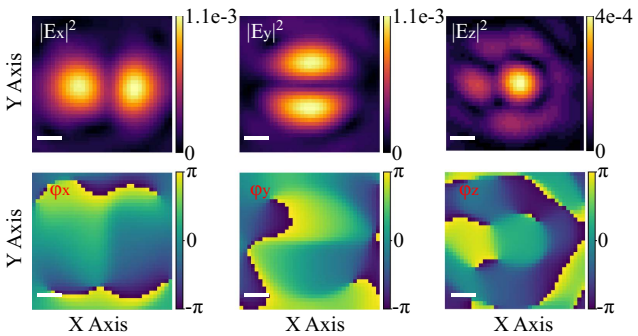

Fig. 4. Reconstructed intensity and phase distributions for the three field components of the radially polarized beam in the focal plane. The intensity distribution results are normalized by total intensity. Scale bars are 150 nm.

3. Discussion and Conclusion

The vectorial measurement with the NV center can be used as feedback to optimize the generation of a complex light field. It will also help to study light–matter interaction at nanoscale. For

the detection without the prior knowledge of the tight focus condition and DPP, more NV centers with axes apart from those in Eqs. (2)–(5) can be used to directly deduce the vectorial distribution of an unknown light field. For example, the measurement with NV centers in a [111]-oriented diamond can provide extra fluorescence patterns under the same light-field pumping. As another method, the diamond plate in this work can be rotated by a specific angle, for example 45° around the z axis, to obtain four more equations about the light-field vector. Benefiting from the additional light field information, the three-dimensional vector distributions can be directly resolved.

According to our results, the high reliability of measurement is guaranteed by the stable fluorescence emission and well-defined symmetry axes of single NV centers. The atomic size of a single NV center enables high spatial resolution and low perturbation for detection. The resolution in this work is limited by the galvo scanning mirror and can be improved in future applications. Compared with the knife-edge technique, our method can detect the phase distribution. Compared with the near-field scanning optical microscope, the probe in our method is stabler, and the light-field detection process can be well predicted. In the future, we will further improve the measurement accuracy of our method. In addition, combining with the fluorescence lifetime measurement, we expect that our method can also be used to detect the local density of an optical state with high spatial resolution.

In conclusion, we propose and demonstrate an efficient method for detecting three-dimensional vector distributions of a light field. The nonresonant excitation of single NV centers with different and well-defined axes is utilized to obtain the vectorial information of a tightly focused light field. Analyzing the fluorescence patterns with the help of the DPP deep neural network, the intensity and phase distributions of the vector light field are reconstructed. The method can help to study light–matter interaction at nanoscale and promote the applications of superresolution imaging, biosensing, photolithography, and optical communication.

Acknowledgement

This work was supported by the Innovation Program for Quantum Science and Technology (No. 2021ZD0303200), the National Natural Science Foundation of China (No. 62225506), the CAS Project for Young Scientists in Basic Research (No. YSBR-049), and the Key Research and Development Program of Anhui Province (No. 2022b13020006).

References

1. J. Li, Y. Zhou, and H. Chen, "Square Maxwell's fish-eye lens for near-field broadband achromatic super-resolution imaging," Chin. Opt. Lett. **20**, 031101 (2022).
2. P. Wang, M. N. Slipchenko, J. Mitchell, C. Yang, E. O. Potma, X. Xu, and J.-X. Cheng, "Far-field imaging of non-fluorescent species with subdiffraction resolution," Nat. Photonics **7**, 449 (2013).
3. E. Rittweger, K. Y. Han, S. E. Irvine, C. Eggeling, and S. W. Hell, "STED microscopy reveals crystal colour centres with nanometric resolution," Nat. Photonics **3**, 144 (2009).
4. P. Banzer, U. Peschel, S. Quabis, and G. Leuchs, "On the experimental investigation of the electric and magnetic response of a single nano-structure," Opt. Express **18**, 10905 (2010).
5. G. Caner, V. Mehdi, and C. Filippo, "Photoinduced magnetic nanoprobe excited by an azimuthally polarized vector beam," ACS Photonics **3**, 2049 (2016).
6. M. Neugebauer, T. Bauer, P. Banzer, and G. Leuchs, "Polarization tailored light driven directional optical nanobeacon," Nano Lett. **14**, 2546 (2014).
7. C. Wan, Q. Cao, J. Chen, A. Chong, and Q. Zhan, "Toroidal vortices of light," Nat. Photonics **16**, 519 (2022).
8. T. Bauer, P. Banzer, E. Karimi, S. Orlov, A. Rubano, L. Marrucci, E. Santamato, R. W. Boyd, and G. Leuchs, "Observation of optical polarization Mobius strips," Science **347**, 964 (2015).
9. H. Larocque, D. Sugic, D. Mortimer, A. J. Taylor, R. Fickler, R. W. Boyd, M. R. Dennis, and E. Karimi, "Reconstructing the topology of optical polarization knots," Nat. Phys. **14**, 1079 (2018).
10. H. Liu, B. Xie, H. Cheng, J. Tian, and S. Chen, "Topological photonic states in artificial microstructures," Chin. Opt. Lett. **19**, 052602 (2021).
11. R. Dorn, S. Quabis, and G. Leuchs, "Sharper focus for a radially polarized light beam," Phys. Rev. Lett. **91**, 233901 (2003).
12. L. Yang, X. Xie, S. Wang, and J. Zhou, "Minimized spot of annular radially polarized focusing beam," Opt. Lett. **38**, 1331 (2013).
13. M. Burresi, R. J. P. Engelen, A. Opheij, D. van Oosten, D. Mori, T. Baba, and L. Kuipers, "Observation of polarization singularities at the nanoscale," Phys. Rev. Lett. **102**, 033902 (2009).
14. T. Grosjean, I. A. Ibrahim, M. A. Suarez, G. W. Burr, M. Mivelle, and D. Charraut, "Full vectorial imaging of electromagnetic light at subwavelength scale," Opt. Express **18**, 5809 (2010).
15. M. Schnell, A. G. Etxarri, J. Alkorta, J. Aizpurua, and R. Hillenbrand, "Phase-resolved mapping of the near-field vector and polarization state in nanoscale antenna gaps," Nano Lett. **10**, 3524 (2010).
16. C. Huber, S. Orlov, P. Banzer, and G. Leuchs, "Influence of the substrate material on the knife-edge based profiling of tightly focused light beams," Opt. Express **24**, 8214 (2016).
17. E. Johlin, J. Solari, S. A. Mann, J. Wang, T. S. Shimizu, and E. C. Garnett, "Super-resolution imaging of light-matter interactions near single semiconductor nanowires," Nat. Commun. **7**, 13950 (2016).
18. K. Guo, M. A. Verschuuren, and A. F. Koenderink, "Superresolution imaging of the local density of states in plasmon lattices," Optica **3**, 289 (2016).
19. A. Cuche, A. Drezet, Y. Sonnefraud, O. Faklaris, F. Treussart, J.-F. Roch, and S. Huant, "Near-field optical microscopy with a nanodiamond-based single-photon tip," Opt. Express **17**, 19969 (2009).
20. A. W. Schell, H. Takashima, T. T. Tran, I. Aharonovich, and S. Takeuchi, "Coupling quantum emitters in 2D materials with tapered fibers," ACS Photonics **4**, 761 (2017).
21. T. Schrder, M. E. Trusheim, M. Walsh, L. Li, J. Zheng, M. Schukraft, A. Sipahigil, R. E. Evans, D. D. Sukachev, C. T. Nguyen, J. L. Pacheco, R. M. Camacho, E. S. Bielejec, M. D. Lukin, and D. Englund, "Scalable focused ion beam creation of nearly lifetime-limited single quantum emitters in diamond nanostructures," Nat. Commun. **8**, 15376 (2017).
22. J. Michl, J. Steiner, A. Denisenko, A. Bülau, A. Zimmermann, K. Nakamura, H. Sumiya, S. Onoda, P. Neumann, J. Isoya, and J. Wrachtrup, "Robust and accurate electric field sensing with solid state spin ensembles," Nano Lett. **19**, 4904 (2019).
23. C. L. Degen, "Scanning magnetic field microscope with a diamond single-spin sensor," Appl. Phys. Lett. **92**, 243111 (2008).
24. M. W. Doherty, N. B. Manson, P. Delaney, F. Jelezko, J. Wrachtrup, and L. C. L. Hollenberg, "The nitrogen-vacancy colour centre in diamond," Phys. Rep. **528**, 1 (2013).
25. J.-C. Jaskula, E. Bauch, S. Arroyo-Camejo, M. D. Lukin, S. W. Hell, A. S. Trifonov, and R. L. Walsworth, "Superresolution optical magnetic imaging and spectroscopy using individual electronic spins in diamond," Opt. Express **25**, 11048 (2017).
26. M. S. J. Barson, L. M. Oberg, L. P. McGuinness, A. Denisenko, N. B. Manson, J. Wrachtrup, and M. W. Doherty, "Nanoscale vector electric field imaging using a single electron spin," Nano Lett. **21**, 2962 (2021).

27. L. P. McGuinness, Y. Yan, A. Stacey, D. A. Simpson, L. T. Hall, D. Maclaurin, S. Prawer, P. Mulvaney, J. Wrachtrup, F. Caruso, R. E. Scholten, and L. C. L. Hollenberg, "Quantum measurement and orientation tracking of fluorescent nanodiamonds inside living cells," Nat. Nanotechnol. **6**, 358 (2011).
28. D. Le Sage, K. Arai, D. R. Glenn, S. J. DeVience, L. M. Pham, L. Rahn-Lee, M. D. Lukin, A. Yacoby, A. Komeili, and R. L. Walsworth, "Optical magnetic imaging of living cells," Nature **496**, 486 (2013).
29. B. Chen, X. Hou, F. Ge, X. Zhang, Y. Ji, H. Li, P. Qian, Y. Wang, N. Xu, and J. Du, "Calibration-free vector magnetometry using nitrogen-vacancy center in diamond integrated with optical vortex beam," Nano Lett. **20**, 8267 (2020).
30. P. R. Dolan, X. Li, J. Storteboom, and M. Gu, "Complete determination of the orientation of NV centers with radially polarized beams," Opt. Express **22**, 4379 (2014).
31. R. J. Epstein, F. M. Mendoza, Y. K. Kato, and D. D. Awschalom, "Anisotropic interactions of a single spin and dark-spin spectroscopy in diamond," Nat. Phys. **1**, 94 (2005).
32. N. Karedla, S. C. Stein, D. Hähnel, I. Gregor, A. Chizhik, and J. O. Enderlein, "Simultaneous measurement of the three-dimensional orientation of excitation and emission dipoles," Phys. Rev. Lett. **115**, 173002 (2015).
33. D. Patra, I. Gregor, and J. Enderlein, "Image analysis of defocused single-molecule images for three-dimensional molecule orientation studies," J. Phys. Chem. A **108**, 6836 (2004).
34. Q. Zhan, "Cylindrical vector beams: from mathematical concepts to applications," Adv. Opt. Photonics **1**, 1 (2009).
35. D. Ulyanov, A. Vedaldi, and V. Lempitsky, "Deep image prior," in *Proceedings of the IEEE Conference on Computer Vision and Pattern Recognition* (2018), p. 9446.
36. H. Reinhard and H. Paul, "Deep decoder: concise image representations from untrained non-convolutional networks," arXiv:1810.03982 (2018).
37. X. Li, T.-H. Lan, C.-H. Tien, and M. Gu, "Three-dimensional orientation-unlimited polarization encryption by a single optically configured vectorial beam," Nat. Commun. **3**, 998 (2012).
38. X. Li, Y. Cao, N. Tian, L. Fu, and M. Gu, "Multifocal optical nanoscopy for big data recording at 30 TB capacity and gigabits/second data rate," Optica **2**, 567 (2015).
39. M. Matthias, R. Valerio, and F. Thomas, "Material processing with pulsed radially and azimuthally polarized laser radiation," Appl. Phys. A **86**, 329 (2007).
40. Q. Zhan, "Evanescent Bessel beam generation via surface plasmon resonance excitation by a radially polarized beam," Opt. Lett. **31**, 1726 (2006).
41. Y. Arita, M. Chen, E. M. Wright, and K. Dholakia, "Dynamics of a levitated microparticle in vacuum trapped by a perfect vortex beam: three-dimensional motion around a complex optical potential," J. Opt. Soc. Am. B **34**, C14 (2017).
42. K. S. Youngworth and T. G. Brown, "Focusing of high numerical aperture cylindrical-vector beams," Opt. Express **7**, 77 (2000).
43. H. Wang, L. Shi, B. Lukyanchuk, C. Sheppard, and C. T. Chong, "Creation of a needle of longitudinally polarized light in vacuum using binary optics," Nat. Photonics **2**, 501 (2008).
44. N. Lukas and H. Bert, *Principles of Nano-Optics* (Cambridge University, 2012).